

# Observations and Magnetic Field Modeling of a Solar Polar Crown Prominence

Yingna Su<sup>1</sup>, Adriaan van Ballegoijen<sup>1</sup>

ynsu@head.cfa.harvard.edu

## ABSTRACT

We present observations and magnetic field modeling of the large polar crown prominence that erupted on 2010 December 6. Combination of SDO/AIA and STEREO\_Behind/EUVI allows us to see the fine structures of this prominence both at the limb and on the disk. We focus on the structures and dynamics of this prominence before the eruption. This prominence contains two parts: an active region part containing mainly horizontal threads, and a quiet Sun part containing mainly vertical threads. On the northern side of the prominence channel, both AIA and EUVI observe bright features which appear to be the lower legs of loops that go above then join in the filament. Filament materials are observed to frequently eject horizontally from the active region part to the quiet Sun part. This ejection results in the formation of a dense-column structure (concentration of dark vertical threads) near the border between the active region and the quiet Sun. Using the flux rope insertion method, we create non-linear force-free field models based on SDO/HMI line-of-sight magnetograms. A key feature of these models is that the flux rope has connections with the surroundings photosphere, so its axial flux varies along the filament path. The height and location of the dips of field lines in our models roughly replicate those of the observed prominence. Comparison between model and observations suggests that the bright features on the northern side of the channel are the lower legs of the field lines that turn into the flux rope. We suggest that plasma may be injected into the prominence along these field lines. Although the models fit the observations quiet well, there are also some interesting differences. For example, the models do not reproduce the observed vertical threads and cannot explain the formation of the dense-column structure.

---

<sup>1</sup>Harvard-Smithsonian Center for Astrophysics, Cambridge, MA 02138, USA.

## 1. INTRODUCTION

Solar prominences are relatively cool structures embedded in the million-degree corona (Hirayama 1985; Labrosse et al. 2010; Mackay et al. 2010). In  $H\alpha$  when viewed above the solar limb, prominences appear as bright structures against the dark background, but when viewed as “filaments” on the solar disk they are darker than their surroundings. We will use the terms “filament” and “prominence” interchangeably in general. A filament is formed in a filament channel, which is defined as a region in the chromosphere surrounding a polarity inversion line (PIL) where the chromospheric  $H\alpha$  fibrils are aligned with the PIL (Foukal 1971; Gaizauskas 1998). Filaments can be found inside activity nest consisting of multiple bipolar pairs of spots (“active region filaments”), at the border of active regions (“intermediate filaments”), and on the quiet Sun (“quiescent filaments”), including the polar crown.

Filaments typically consist of three structural components: a spine, barbs, and two extreme ends (Martin 1998; Lin et al. 2008; Lin 2011). The spine runs horizontally along the top of the filament, although there may be sections along the filament where the spine is nearly invisible. The barbs protrude from the side of the filament and when observed closer to the limb, the barbs are seen to extend down from the spine to the chromosphere below. The ends, also called “legs”, may be a collection of threads that appear to terminate at a single point or at multiple points. When a quiescent filament is viewed with high resolution on the solar disk,  $H\alpha$  observations indicate that each of these three structural components consist of thin thread-like structures (Lin et al. 2008; Lin 2011). In active regions the thin filament threads often appear to be mostly horizontal (Okamoto et al. 2007; Lin et al. 2008), while quasi-vertical threads (“hedgerows”) are often seen in the quiescent prominences (Berger et al. 2008, 2010; Chae et al. 2008; Heinzel et al. 2008). Prominence plasma is highly dynamic, exhibiting horizontal (Chae et al. 2008) or vertical (Berger et al. 2008) flows. The flows reported so far are either unidirectional (Berger et al. 2008; Chae et al. 2008) or bidirectional (Zirker et al. 1998; Lin et al. 2003). The latter is known as counter-streaming.

The magnetic field plays a primary role in filament formation, stability, and eruption (Priest 1989; Tandberg-Hanssen 1995; Mackay et al. 2010). However, the magnetic structure of prominences is still not fully understood, with many observations and theoretical models differing on the exact nature of the magnetic field. Various models for prominence magnetic structure can be summarized as follows. In most of the models, filament plasmas are assumed to be located near the dips of magnetic field lines. These models can be classified as “sheared arcade model” (Antiochos et al. 1994; DeVore & Antiochos 2000; Aulanier et al. 2002) and “flux rope model”, (Kuperus & Raadu 1974; Pneuman 1983; Priest et al. 1989; van Ballegooijen & Martens 1989; Rust & Kumar 1994; Low & Hundhausen 1995; Aulanier et al. 1998; Chae et al. 2001; van Ballegooijen 2004; Gibson et al. 2006; Dudík et al. 2008). In

these models, the prominence plasmas are embedded in a large sheared arcade or a flux rope that lie horizontally above the PIL. Flux rope models may be split into two categories: weakly twisted flux rope and highly twisted flux rope. Weakly twisted flux rope models are similar to sheared arcades with one key difference as argued by Mackay et al. (2010). For flux rope models the flux rope and overlying arcade are independent flux systems with a separatrix surface between them. In contrast, for a sheared arcade model only a single flux system exists. In addition to the above mentioned 3D global models, there are also two other dip models which focus on the local support of vertical threads in hedgerow prominence, i.e., “sagged horizontal fields model” (Chae et al. 2008; Chae 2010) and “tangled magnetic field model” (van Ballegoijen & Cranmer 2010). In the earlier model, the vertical threads are stacks of plasma supported against gravity by the sagging of initially horizontal magnetic field lines. In the latter model, tangled fields exist in a vertical current sheet of small width that is confined by the vertical fields on either side of the sheet. Neither of these models describes the global 3D topology of the magnetic field supporting the filament. In contrast to models mentioned above, the “field aligned thread model” developed by Lin et al. (2008); Lin (2011) does not contain dipoles. This model is a 3D empirical magnetic model based on high-resolution  $H\alpha$  observations and is based on the assumption that the observed fine scale structures are parallel to the magnetic field. In this model, the filament plasma is located on magnetic arches that are highly sheared in the direction along the PIL. Some field lines run along the entire length of the filament and outline the filament “spine”. Other shorter ones run partially along the spine, but spread out from it and connect down to minority polarity elements on either side of the PIL. These shorter structures represent the filament barbs. In this case, the plasma is supported by MHD waves. However, relatively high frequencies and wave amplitudes are required, and it is unclear why such waves would not lead to strong heating of the prominence plasma.

The purpose of the present paper is to analyze observations of a quiescent prominence, and to develop 3D models of its magnetic structure. Filaments in active regions have been modeled extensively in the past. Several authors have developed non-linear force-free field (NLFFF) models which are based on magnetic observations. For example, Régnier & Priest (2007) construct NLFFF models by “extrapolating” observed photospheric vector fields into the corona (also see Régnier et al. 2002; Canou & Amari 2010). van Ballegoijen (2004) developed an alternative method for constructing NLFFF models of filament flux ropes. The method involves inserting a flux rope into a potential field based on an observed photospheric magnetogram, and then evolving the field in time to an equilibrium state using magneto-frictional relaxation. This method has been used by Bobra et al. (2008) and Su et al. (2009a,b, 2011); Asgari-Targhi & van Ballegoijen (2012) to study active regions with filaments, and by Savcheva & van Ballegoijen (2009); Savcheva et al. (2012a,b) to study the

evolution of soft X-ray sigmoid. The papers mentioned above suggest that the observed active region filaments can be well explained by a flux rope model. In this paper we apply this flux rope insertion method to a quiescent prominence for the first time.

## 2. Observations

### 2.1. Data Sets and Instruments

A large polar crown prominence was observed in the period December 1–6 in 2010, by the Atmospheric Imaging Assembly (AIA, Lemen et al. 2012) aboard the *Solar Dynamics Observatory* (SDO), as well as the STEREO\_B (Behind)/EUVI (Wuelser et al. 2004; Howard et al. 2008). Synoptic observations by the X-Ray Telescope (XRT, Golub et al. 2007; Kano et al. 2008) aboard *Hinode* (Kosugi et al. 2007) and  $H\alpha$  observations by the Kanzelhöhe Solar Observatory (KSO) are also included in the study. The photospheric magnetic field information is provided by the Helioseismic and Magnetic Imager (HMI, Schou et al. 2012) aboard SDO and SOLIS (Synoptic Optical Long-term Investigations of the Sun).

The large prominence erupted around 14:18 UT on 2010 December 6. This prominence eruption is associated with a CME, which has a linear speed of  $538 \text{ km s}^{-1}$ , according to the SOHO LASCO CME catalog<sup>1</sup>. Detailed studies on the prominence eruption are presented by Su & van Ballegoijen (2012b); Thompson (2012). In the current paper, we present the structure and dynamics of the prominence before and after the eruption.

### 2.2. Structure and Dynamics of the Prominence and Surroundings

#### 2.2.1. Prominence Structure and Dynamics before the eruption

Figures 1–2 shows SDO/AIA observations of the evolution of the prominence within six days (December 1–6) prior to the eruption. The images on the left, middle, and right columns are taken at  $304 \text{ \AA}$ ,  $171 \text{ \AA}$ , and  $193 \text{ \AA}$ , respectively. Note that artificial color is used for the on-line only figures. Red color is used for the images taken at  $304 \text{ \AA}$  by both AIA and EUVI, while  $171 \text{ \AA}$  images by AIA are yellow. Images at  $193 \text{ \AA}$  by AIA are dark yellow, while EUVI images at  $195 \text{ \AA}$  are green. Moreover, both  $193 \text{ \AA}$  and  $195 \text{ \AA}$  provide similar spectral information. On December 1, the prominence is observed at the east limb and contains mainly horizontal threads shown as emission at  $304 \text{ \AA}$  (white arrows in Figure 1a).

---

<sup>1</sup>[http://cdaw.gsfc.nasa.gov/CME\\_list/](http://cdaw.gsfc.nasa.gov/CME_list/)

A dark feature is also seen in absorption at all three wavelengths (black arrows in Figures 1a–1c). On December 2 and 3, the first part of the prominence rotated onto the disk, and the prominence at the limb becomes more complex. One can see some dark vertical threads with overlying bright horizontal threads as shown in Figures 1d and 1g. Images at 304 Å shows the vertical threads either in emission or absorption. The dark vertical threads are better seen at 171 Å and 193 Å. Sometimes, bright emission in the prominence is also visible at 171 Å (e.g., Figure 1h). This bright emission in 171 Å is analyzed by Parenti et al. (2012). Figure 2 shows the prominence from December 4 to December 6. The filament on the disk shown at 171 Å and 193 Å appears to be much narrower than the one shown at 304 Å. SDO/HMI observations (black and white contours in Figure 2h) show that the underlying magnetic fields are positive on the southern side and negative on the northern side of the filament.

The AIA observations suggest that this prominence can be divided into three parts: a region with mostly horizontal threads (Part I), a region with horizontal threads overlying the vertical threads (Part II), and a region with mostly vertical threads (Part III). This prominence contains several different features which are marked as numbers in Figure 2g. Part I is located in the active region, which is on the northwestern side of the black dashed line in Figure 2g. The horizontal threads (marked as “1” in Figure 2g) in Part I are best viewed at the limb in Figure 1a. Part II is located between the black and white dashed lines as shown in Figure 2g. The limb view of this region is shown in the images from December 2 to December 6 in Figures 1–2. Feature “2” is a dense column composed of dark vertical threads which appear to be perpendicular to the overlying horizontal threads. The limb view of Part II displays an arch-like structure. The two feet of this arch (marked as “4” and “6”) contain mostly quasi vertical threads, while the top of the arch is composed of mostly horizontal threads (feature “3”). Note that the threads in feature 4 are not vertical, and the prominence spine appears to tilt towards the South. Feature 5 refers to the hole located below the top of the arch. Part III is located on the northern side of the white dashed line. This part is composed of mostly vertical threads (feature “8”) overlying a bubble-like structure (feature “7”). Feature “9” refers to a horn-like structure located above the vertical threads. All prominence structures are clearly visible at 304 Å, while only parts of the prominence are seen as absorption in 171 Å and 193 Å, which best reveal the fine structure of the vertical threads. Note that some features are also visible as emission in 171 Å.

The aforementioned AIA observations reveal the filament while it rotating from the east limb to the disk. STEREO\_B views this filament as it rotating from the disk to the west limb. Figures 3–4 show the filament from December 1 to December 6 at 304 Å and 195 Å observed by EUVI aboard STEREO\_B. On December 1, the filament displays a dark long and narrow structure. The filament on the east appears to grow wider and thicker with time. The black

dashed line in Figure 4 divides the filament into two parts. The western part of the filament (active region part) contains mainly horizontal threads, while the eastern part (quiet Sun part) contains mainly quasi-vertical threads. Unlike AIA, EUVI observations do not reveal the horizontal threads located on top of the quasi-vertical threads. A comparison of Figures 4c and 4e shows that the active region part of the filament appears to rise up on December 6.

Figure 5 shows the filament observed at  $H\alpha$  by KSO within four different days prior the eruption.  $H\alpha$  observations show similar filament structures as those found at the EUV channels by AIA. A comparison of Figures 5c and 5d shows that most part of the active region filament (marked as black arrows) disappeared before the eruption on December 6. This is consistent with the rise of the active region filament as observed by EUVI.

The prominence before the eruption is very dynamic. Horizontal counter-streaming along the top of the arch as shown in Figure 2g is clearly seen in the AIA 304 Å observations (see video 1). Downflows are also observed in part of the vertical threads. Part of the vertical threads are just waving around without clear flows as shown in the AIA 193 Å observations. EUVI observations (video 2) show that the filament material is ejected from the active region part to the quiet Sun part. This ejection leads to the horizontal oscillations of the vertical threads and the formation of a dark tree-like structure (marked using white arrows in Figure 4) near the border between the active region and the quiet Sun.

### 2.2.2. Dense Column Structure

Figure 6 shows comparisons of the AIA and EUVI observations of the filament on December 6. The field of view of the AIA and EUVI images are shown as black boxes in Figure 2i and Figure 4f, respectively. Figures 1–2 and Figures 3–4 suggest that the appearance of the filament is very different in AIA and EUVI observations. Therefore, to compare different filament features observed by the two instruments, we first identify a series of bright-point like features, which are marked as numbers in Figure 6. A careful comparison shows that the dense column observed by AIA corresponds to the tree-like structure observed by EUVI. This dense column is formed by the strong accumulation of quasi-vertical threads (marked as white arrows in all images).

### 2.2.3. The Structure around the Prominence

The prominence is located in a very narrow filament channel, which is best observed at 195 Å by EUVI as shown in Figure 3. Straight faint features (traced using white lines

in Figure 3f) are observed on the two sides of the channel. These features may refer to the lower legs of the overlying coronal arcades. Near the quiet Sun part, one can see some bright curved features (traced using black lines in Figure 3f), which are located on the northern side of the filament channel. No clear counterparts of these features can be identified on the southern side of the channel. This emission asymmetry that was first identified by Su et al. (2010) is also clearly visible in AIA observations, see Figures 2i and 6. However, these bright curved features appear to be straight in the AIA view. To have a better understanding on this asymmetry, we trace these features back when they are observed at the east limb by AIA. Figure 7 shows AIA 171 Å images on December 4–6. Each image is the average of 30 images taken within 6 minutes. All images are contrast enhanced using a radial filter technique developed by S. Cranmer (2010, private communication). The top images show bright loops which start from the northern side of the filament channel (white arrows), arch over the filament, and finally disappear behind the filament or join in the filament. Evolution of this type of loops from December 3 to December 6 are shown in the online video (video 3). The existence of these loops is consistent with the emission asymmetry in the sense that they do not have clear footpoints on the southern side of the filament channel. Su et al. (2010) interpreted these bright curved features as magnetic field lines that turn into the flux rope.

The bottom images in Figure 7 show highly sheared bright loops (white arrows) that go above the prominence. However, it is not clear where these loops end. Figure 7d also shows several bright horn-like features (black arrows) located right above the vertical prominence threads. This observation appears to suggest that some part of the flux rope lies above the prominence vertical threads.

Figure 8 shows images of the prominence at different channels observed by SDO/AIA and Hinode/XRT on 2010 December 4. A clear cavity surrounding the prominence can be seen in the two XRT images. The AIA image at 335 Å which is an average over 4 minutes shows similar structure as observed by XRT. No clear cavity can be identified in the other three EUV channels, i.e., 304 Å, 171 Å, and 193 Å. The AIA image at 335 Å (Figure 8d) shows that the dark filament lies on the southern edge of the cavity rather than at the center. We also can see that the bright coronal arcades surrounding the cavity appear to be asymmetric, i.e., the bright structure on the northern side is brighter than that on the southern side. This asymmetry is also clearly visible in the two XRT images (Figures 8e–8f).

Martin & McAllister (1996) found that there is a one-to-one correspondence between the dextral/sinistral orientation of the filament channel and the skew of the overlying coronal arcade. This implies that the axial magnetic field within filaments points in the same

direction as that of the surrounding corona. As viewed from the positive polarity side, for a sinistral filament the axial component of the field in the arcade points to the left, and vice versa (i.e., Figure 1 in McAllister et al. 2002). Figure 9 shows the post-eruption arcade above the erupted filament observed at 335 Å by AIA on 2010 December 7. As shown in Figure 2h, the positive polarity (white patches) is located on the southern side of the filament channel. This orientation of the arcade suggests that this filament is a sinistral filament, according to the aforementioned definition.

#### 2.2.4. Prominence Structure after the Eruption

The prominence eruption on December 6 is a partial eruption, which means that part of the filament survived the eruption. Figure 10 shows the east end of the quiescent prominence after the eruption. SDO observes this prominence at the east limb (left column), while STEREO\_B views it on the disk (right column). The side view of this prominence by AIA suggests that it contains mainly vertical threads. Images at 304 Å shows the vertical threads either in emission or absorption. Dark quasi-vertical threads are seen in absorption at both 171 Å and 193 Å. In 171 Å, one can also see a bright horizontal structure located on top of the dark vertical threads. The filament displays a thin dark structure, when viewing it from the top as shown in the STEREO\_B observations. The width of the filament at 304 Å (Figure 10b) is larger than that at the other two EUV channels (Figures 10d–10e). Without the different point of view from SDO, it is very difficult for us to imagine that this thin dark filament contains vertical threads. It looks very similar to the active region filament which contains mainly horizontal threads. This thin dark filament structure may be the horizontal filament threads located on top of the vertical threads. Another possibility is that it is just the accumulation of the lined up dark vertical threads, and there are no horizontal threads. The spatial resolution of EUVI does not allow us to distinguish whether there are overlying horizontal threads or not.

### 3. Models for the Observed Prominence

It has been suggested that Quiescent Prominences (QPs) are located in helical flux ropes that lie horizontally above filament channels on the quiet Sun (e.g., Rust & Kumar 1994; Low & Hundhausen 1995). The prominence plasma is assumed to be located at dips in the helical field lines. In this section we construct three-dimensional (3D) flux rope models for the observed prominence, then we compare the models with AIA and EUVI observations. The coronal arcade overlying a QP flux rope is thought to play an important role in its



equilibrium and stability. To have stable equilibrium, the magnetic tension of the overlying arcade must balance the magnetic pressure of the flux rope. If the overlying fields are too weak, the flux rope will rise and expand into the heliosphere. Therefore, an important open question is whether QP flux ropes can exist in stable equilibrium with their surroundings. The overlying fields are anchored in the quiet photosphere, which often has mixed polarity with only a small excess of one polarity over the other. It is unclear how effective such mixed-polarity fields can be in anchoring QP flux ropes. The purpose of the present modeling is to determine whether the observed QP can be explained in terms of a stable flux rope model.

### 3.1. Methodology

In this subsection we describe how the models are constructed. In the last few years, we have developed various tools for modeling non-potential magnetic fields in the solar corona, called the Coronal Modeling System (CMS). Its main purpose is to construct NLFFF models of the coronal magnetic field. The models are constructed by inserting a magnetic flux rope into a potential-field model of the region and then applying magneto-frictional relaxation (MFR). This “flux rope insertion” method is quite flexible and provides information about the stability of the resulting magnetic fields (Su et al. 2011). In the present study we apply this flux rope insertion method to a quiescent prominence for the first time.

The observed QP is more than a solar radius in length, and the model needs to include the overlying coronal arcade, so a large simulation domain with spherical geometry is required. However, we also need to resolve the mixed-polarity fields on the quiet Sun, which requires high spatial resolution (a few Mm or better). To achieve these goals, the CMS code uses variable grid spacing: at low heights the grid spacing is about  $0.002 \cos \lambda R_\odot$ , where  $\lambda$  is the latitude, but at larger heights the cell size is increased by powers of 2. The high-resolution (HIRES) computational domain extends about  $117^\circ$  in longitude,  $48^\circ$  in latitude, and up to  $2.41 R_\odot$  from Sun center. The magnetic field  $\mathbf{B}(\mathbf{r})$  in this domain is described in terms of vector potentials,  $\mathbf{B} = \nabla \times \mathbf{A}$ .

The lower boundary condition for the HIRES region is derived from line-of-sight (LOS) photospheric magnetograms obtained with the SDO/HMI. Since the prominence is observed near the east limb, we have to use magnetograms that are taken several days after the prominence eruption on December 6. We combine four magnetograms taken on 2010 December 8, 9, 10 and 11 (each at 14:00 UT) to construct a high-resolution map of the radial component  $B_r$  of magnetic field as function of longitude and latitude at the lower boundary of the HIRES region. We also use a SOLIS synoptic map of  $B_r$  to compute a low-resolution global potential field, which provides the side boundary conditions for the HIRES domain, and also

allows us to trace field lines that pass through the side boundaries of the HIRES region.

The HIRES magnetic map is shown in Figure 11a. Note that outside the active region the field has mixed polarity with dominantly positive polarity on the south side of the PIL and negative polarity on the north side. Based on this map alone it is difficult to recognize exactly where the PIL is located. Therefore, we used co-aligned AIA images and HMI magnetograms to locate the base of the prominence/filament on the magnetic map (blue curve in Figure 11). This curve is the path along which the flux rope will be inserted into the model. At the two ends of the path (blue circles) the flux rope is anchored in the photosphere. Figure 11b shows the zoomed-in view of magnetic map shown in Figure 11a (red and green contours) overlaid on the HMI LOS magnetogram taken at 14:00 UT on December 6 (black and white image). This figure shows that there is no significant differences between the magnetic fields taken before the eruption (on December 6) and after the eruption (December 10 and 11). One may notice some shift in individual magnetic patches, but no significant flux emergence and cancellation can be identified. Moreover, the polarity inversion line appears to remain the same. It suggests that using HMI data several days after the eruption to model the prominence just before the eruption is reasonable.

The methodology of flux rope insertion has been described elsewhere (e.g., Bobra et al. 2008; Su et al. 2009b), so only a brief summary will be given. First, the potential field is computed from the HIRES and global magnetic maps. Then by appropriate modifications of the vector potentials a “cavity” is created above the selected path, and a thin flux bundle (representing the axial flux of the flux rope) is inserted into the cavity. Circular loops are added around the flux bundle to represent the poloidal flux of the flux rope. Then MFR is applied to drive the magnetic field toward a force-free state. MFR is basically an evolution of the magnetic field according to the magnetic induction equation with the velocity taken to be proportional to the Lorentz force (e.g., Yang et al. 1986; van Ballegooijen et al. 2000). The magnetic diffusion is kept as small as possible, so that the magnetic topology of the field is approximately conserved (some diffusion is needed to prevent numerical artifacts). If the axial and/or poloidal fluxes of the flux rope are too large, the model will not reach an equilibrium state but the field will keep expanding and moving to large heights, similar to what happens on the real Sun during an eruption. In this paper we are interested only in stable configurations, so we seek values of the model parameters that produce stable NLFFFs. In previous work we usually iterated the induction equation about 30,000 times, but we found that for QP flux ropes this is not enough to reach an equilibrium state. For the models presented here we use 90,000 iterations.

For the models discussed in this paper, two magnetic sources with fluxes of  $\pm 2 \times 10^{20}$  Mx were added to the  $B_r$ -map at the two ends of the filament path in order to enhance

the stability of the flux rope. The axial flux near the ends of the (blue) path equals the flux of the sources ( $\Phi_{\text{axi}} = 2 \times 10^{20}$  Mx). The axial field points to the left (east) as seen by an observer looking at the QP from the south polar region, which has positive polarity. Therefore, the flux rope has *sinistral* orientation, consistent with the observed skew of the post-eruption arcades (see Figure 9) and with the hemispheric pattern of chirality of filament channels (Martin et al. 1994).

The observations clearly show a filament within the active region, and the STEREO\_B observations provide constraints on its height. Preliminary modeling showed that in order to reproduce the observed active region filament the axial flux of the flux rope must exceed a certain minimum value:  $\Phi_{\text{axi}} > 6 \times 10^{20}$  Mx. However, such values were found to be too high for the eastern part of the filament overlying the quiet Sun (longitude  $< 0$  in Figure 11). Axial fluxes in excess of  $4 \times 10^{20}$  Mx lead to the eruption of the eastern part as the surrounding quiet-Sun fields are too weak to anchor the flux rope to the photosphere. Therefore, we must consider models in which the axial flux  $\Phi_{\text{axi}}$  varies with position along the flux rope. This is achieved by adding magnetic flux to (or removing flux from) the flux rope at certain places along the filament path. These places are indicated by the yellow “barbs” in Figure 11. In fact, real filaments have barbs that may indeed be sites where magnetic flux enters or leaves the main filament (e.g., Lin 2011). In Figure 11, the circle at the end of a yellow line segment indicates the source (or sink) of the added flux. As we follow the (blue) filament path from right to left in the figure, the two barbs near longitude  $+40^\circ$  each add  $3 \times 10^{20}$  Mx to the flux rope, and the three barbs near longitude  $+5^\circ$  each subtract  $2 \times 10^{20}$  Mx. Therefore, the axial flux in the active region (in between the two sets of barbs) is  $8 \times 10^{20}$  Mx, and the axial flux on the quiet Sun (outside the two sets of barbs) is  $2 \times 10^{20}$  Mx. The barbs near  $+5^\circ$  are put on the south side of the PIL in order to force the turned-out field lines to arch over the flux rope on their way to the negative polarities on the north side. We find that this initial setup leads to stable models that are in rough agreement with the observations.

### 3.2. Modeling Results and Comparison with Observations

In this paper we focus on models representing possible magnetic configurations just prior to the eruption that started at 14:20 UT on 2010 December 6 (as discussed in section 3.1, the models are actually based on magnetograms taken several days later). Two values for the poloidal flux  $F_{\text{pol}}$  of the flux rope are considered:  $1 \times 10^{10}$  Mx  $\text{cm}^{-1}$  (Model 1), and  $2 \times 10^{10}$  Mx  $\text{cm}^{-1}$  (Model 2). Figure 12 shows results from the NLFFF models and a comparison with AIA observation. The top panels show the two models, projected onto the plane of the sky as seen from SDO. The bottom panels show co-aligned images of the Sun taken with

AIA in the 193 Å and 304 Å passbands. The colored curves in the top panels are magnetic field lines traced through the model, and the blue features indicate the locations of dips in the field lines, i.e., sites where the field lines are locally horizontal and curved upward (light blue for low-lying dips, darker blue at larger heights). The red and green contours show the magnetic flux distribution on the photosphere. Note that the field lines in Figure 12b are more twisted than those in Figure 12a, which is due to the difference in the poloidal flux of the inserted flux rope. Both models reproduce more or less the observed prominence height (about 70 Mm) as seen in the AIA 304 Å image (see Figure 12d). This means that the modeled flux rope is sufficiently thick, and the axis of the flux rope lies at sufficiently large height to provide a reasonable model for the observed prominence everywhere along its length. In the remainder of this paper we only consider the model with poloidal flux  $F_{\text{pol}} = 10^{10} \text{ Mx cm}^{-1}$ , i.e, Model 1.

Figure 13 shows a zoomed-in view of the middle part of Figure 12a. At this resolution the blue features resolve into small blue dots that indicate the locations of field-line dips. The dots lie on surfaces where the radial component of magnetic field vanishes,  $B_r(r, \theta, \phi) = 0$ , where  $r$ ,  $\theta$  and  $\phi$  are spherical coordinates. Note that the dots in Figure 13 make patterns of horizontal and quasi-vertical lines. These patterns should not be taken too seriously because they are an artifact of the way the dips are chosen. Specifically, we locate the intersections of the surface  $B_r = 0$  with the “edges” of the 3D grid on which the magnetic field  $\mathbf{B}$  is defined (actually, the dots are short line segments indicating the direction of the horizontal field at the dips, but this is not visible in Figure 13). Therefore, the patterns of horizontal and vertical lines are created by interference with the 3D grid. However, we also see “ridges” in Figure 13 where the density of dots is higher than elsewhere. This indicates that the surface of dips is strongly warped, and in some places our line-of-sight is tangential to this warped surface. The warping of the  $B_r = 0$  surface is due to the uneven distribution of magnetic sources on the photosphere (e.g., Aulanier & Démoulin 2003). It has been suggested that the quasi-vertical threads in quiescent prominences may be due to such ridges (e.g., Heinzel & Anzer 2006; Dudík et al. 2008). However, we find that in our model the ridges are not always vertical, and the number of ridges per unit length along the prominence is far too small for the ridges to be identified with the observed vertical threads, which usually are densely packed. Therefore, the distribution of field-line dips in our NLFFF model does not reproduce the observed quasi-vertical threads.

Figure 14 shows a comparison of Model 1 with AIA and EUVI observations of the coronal arcade surrounding the prominence. The top panels show the same set of field lines seen from two different viewing angles: (a) from SDO, and (b) from STEREO\_B. The bottom panels show images in AIA 193 Å and EUVI 195 Å, which are dominated by emission in Fe XII 195 Å. These images show thin threads and fans that presumably are aligned with the local

magnetic field. On the quiet Sun the plasma density drops rapidly with height due to the gravitational stratification of plasma along the magnetic field lines. The Fe XII ion is formed at temperatures of about 1.5 MK, and the density scale height for such plasma in the low corona is about 75 Mm. The emissivity in Fe XII 195 Å is proportional to density squared, which decreases even more rapidly with height. Therefore, we expect that in observations on the solar disk the Fe XII 195 Å emission will be dominated by plasma in the lower parts of coronal loops. Accordingly, in Figures 14c–14d we overplot the lower parts of the field lines as blue line segments shown in 14a–14b; only heights less than  $0.07 R_{\odot}$  (49 Mm) are shown. Close inspection of these images shows that the orientation of the line segments is roughly in agreement with the directions of the thread-like structures seen by AIA and EUVI. In particular, the model reproduces the bright features on the northern side of the PIL. Some of these threads are located on field lines that turn into the flux rope as we follow its path from east to west. This comparison between model and observations indicates that Model 1 reproduces the surrounding magnetic fields quite well. This model also confirms our previous interpretation of the emission asymmetry on the two sides of the quiescent filament channels. Those bright curved features on the north side of the PIL represent the lower part of the magnetic field lines that turn into the flux rope (Su et al. 2010).

Figure 15 shows the magnetic field strengths at dips in the field lines, plotted as function of the height  $z$  of the dips above the photosphere. The prominence plasma is assumed to be located at such dips. All positions along the filament channel are included in this plot, except the two ends of the flux rope where the rope is anchored in the photosphere. The heights of the dips range up to 70 Mm, and the field strengths range from 40 G in the active region to 4.5 G in the quiescent part of the filament. The values of field strength are consistent with measurements of prominence magnetic fields using the Hanle effect (e.g., Bommier et al. 1994), and with results from constant- $\alpha$  magnetohydrostatic modeling (Aulanier & Démoulin 2003). The plasma pressure in quiescent prominences lies in the range 0.1 - 2.0 dyne cm<sup>-2</sup> (Jensen & Wiik 1990; Heinzel & Anzer 2006), so a magnetic field strength of 4.5 G corresponds to a plasma  $\beta$  in the range 0.12 - 2.5, where  $\beta$  is the ratio of plasma- and magnetic pressures. Heinzel & Anzer (2006) have shown that when  $\beta > 1$  the weight of the prominence plasma will significantly distort the shape of the magnetic field lines; such effects are not taken into account in the present models. From the above estimates for  $\beta$  it is clear that gravity may significantly deepen the field-line dips in the quiescent prominence compared to our NLFFF model. Heinzel & Anzer (2006) have developed 2D models of prominence threads supported by gravity-induced dips in the field lines. In the active region the effects of gravity are expected to be minor ( $\beta < 0.03$ ).

There are interesting differences between our models and observations. First, as mentioned above the AIA observations show thin vertical threads in the prominence near the

limb, but our models do not have any such features in either the shapes of the magnetic field lines or the distribution of field-line dips. This is not surprising because our NLFFF models do not include the effects of plasma pressure and gravity, which likely are responsible for producing the vertical threads (Kippenhahn & Schlüter 1957; Heinzel & Anzer 2001; Low & Petrie 2005; Hillier et al. 2012). Second, the model cannot explain the formation of the dense-column structure.

The PIL is shown as a blue curve in Figure 11, and as a red curve in Figure 12d. Note that the filament spine is displaced to the South relative to the PIL in Figure 12d, whereas the base of the filament appears to be located near the PIL. Therefore, the prominence does not lie vertically above the PIL, but it tilted to the South. This tilt is not reproduced in either Model 1 or Model 2. In the models the flux rope lies directly above the PIL, which is where the flux rope is inserted into the model. We create another model (Model 3) in order to see whether we can reproduce the tilt of the prominence by changing the path where the flux rope is inserted. Figure 16 shows top view of the field line dips (blue features) from Model 1 and Model 3. Model 3 has the same parameters as Model 1 except that the filament path (red curve) is displaced to the south in the longitude range between  $-35^\circ$  and  $-5^\circ$ . The path in Model 3 is along the filament spine rather than the filament base as used in the other two models (see Figure 12d). Figure 16b suggests that the field line dips are pushed back to the PIL (filament base) after 90000-iteration MFR, though the flux rope is originally inserted along the filament spine (red curve). Therefore, the tilt of the filament cannot be better reproduced by changing the path of the flux rope. This absence of tilt is also not due to any lack of convergence of the MFR; there simply is no force in the model to push the flux rope sideways. Therefore, the observed tilt of the QP is somewhat of a mystery.

Figure 17 shows comparison of the observed cavity and magnetic field lines from Model 1. The AIA image in Figure 17a shows that the cavity is tall and narrow rather than a half circle-like shape. The size and shape of the model flux rope is represented by the inner most dark blue line shown in Figure 17b. A comparison of these two figures suggests that the observed cavity is taller than the modeled flux rope. The observations show that the bright features surrounding the cavity are nearly vertical with respect to the solar limb. However, the lower part of the modeled field lines on the south side of the cavity are much more inclined in comparison to the observations.

The two models presented in Figure 12 lie at the edge of the stable regime. Indeed, an eruption does occur starting at 14:20 UT, shortly after the time for which the models are constructed. However, the eruption involves only the western part of the QP; the eastern part remains behind and is apparently quite stable (see Figure 10). This partial eruption is difficult to understand on the basis of our models: the flux rope extends along the full length

of the QP, and therefore we expect that the eruption should remove the entire flux rope. This leads us to question the validity of the flux rope model for describing the magnetic structure of this QP.

#### 4. Discussion and Conclusions

A large polar crown prominence partially erupted on 2010 December 6. To understand the magnetic support of the prominence, we focus on the structure and dynamics of the prominence before and after the eruption. The 6-day SDO/AIA observations of the filament near the east limb before the eruption suggest that this filament can be divided into 3 parts. The active region part near the west end contains mainly horizontal threads. The middle part near the quiet Sun contains vertical threads with overlying horizontal threads. While the east end of the prominence that survived the eruption appears to be composed of mainly vertical threads. The post-eruption limb observations by AIA suggest that the prominence left behind contains mainly vertical threads, while a regular thin dark filament structure appears in the on-disk observations by EUVI. This thin dark filament structure may be the horizontal filament threads located on top of the vertical threads. Another possibility is that it is just the accumulation of the lined up dark vertical threads, and there are no horizontal threads. Such structure, consisting of horizontally aligned threads, was reported by Schmieder et al. (2004) for another filament. Corresponding  $H\alpha$  appearance of such threads was discussed by Heinzel & Anzer (2006).

STEREO/EUVI observes straight and faint features representing the lower legs of the overlying coronal arcades on the two sides of the filament channel. On the quiet Sun part, bright features with no clear counterparts are also identified on the northern side of the channel. This emission asymmetry is consistent with the existence of loops that originates from the northern side of the channel, then arch over the filament and disappear or join in the filament as shown in earlier limb observations at  $171 \text{ \AA}$  by AIA. A clear cavity corresponding to the filament channel is observed on December 4 at  $335 \text{ \AA}$  by AIA and XRT. The observations suggests that the filament is located on the southern edge of the cavity rather than at the center. The bright features (lower legs of the coronal arcades) on the north side of the cavity are brighter than those on the south side. The skew of the post-eruption arcade suggests that this filament is sinistral.

The prominence before the eruption is very dynamic. AIA observes horizontal counter-streaming overlying the vertical threads. STEREO\_B/EUVI observes filament material ejection from the active region part to the quiet Sun part. This ejection leads to strong oscillations of the vertical threads and the formation of a dense column near the border between

the active region and quiet Sun. The dense column refers to strong accumulation of dark vertical filament threads.

Using the flux rope insertion method developed by van Ballegooijen (2004) we construct two non-linear force-free field models. The poloidal flux ( $1 \times 10^{20}$  Mx  $\text{cm}^{-1}$ ) in Model 1 is half of that in Model 2, so the flux rope in Model 1 is less twisted. In both models, the axial fluxes are  $8 \times 10^{20}$  Mx and  $2 \times 10^{20}$  Mx in the active region and quiet Sun, respectively. Since the prominence is observed at the east limb, the models are constructed based on the combined LOS photospheric magnetogram observed by SDO/HMI several day after the prominence eruption. Both models lie at the edge of the stable regime.

Our models match some of the observed features quiet well. For example, the height and location of the field line dips in our models appear to match those of the prominence threads, though the narrow vertical thread-like structure is not reproduced in our model. The lower part of the magnetic field lines from our models can replicate the bright features on the two side of the filament channel quite well. Our model also confirms our previous interpretation of the emission asymmetry on the two sides of the channel on the quiet Sun (Su et al. 2010). This emission asymmetry is due to the fact that some of the bright features on the northern side (the brighter side) of the channel represent the field lines that turn into the flux rope. Therefore, no counterparts of these features can be found on the southern side of the channel. We suggest that plasma may be injected into the prominence along the aforementioned field lines that turn into the flux rope, since these field lines start from the photosphere. This is consistent with the thermal nonequilibrium mechanism for prominence formation as suggested by Antiochos, Karpen, and colleagues (e.g., Antiochos & Klimchuk 1991; Karpen et al. 2005; Luna et al. 2012). In this model, localized heating above the flux tube footpoints produces evaporation of the chromospheric plasma, which condenses in the coronal part of the flux tube.

Acknowledgments: We thank the anonymous referee for valuable comments to improve this paper. Hinode is a Japanese mission developed and launched by ISAS/JAXA, with NAOJ as domestic partner and NASA and STFC (UK) as international partners. It is operated by these agencies in co-operation with ESA and the NSC (Norway). We thank the team of SDO/AIA, SDO/HMI, STEREO/EUVI, Hinode/XRT, KSO, and SOLIS for providing the valuable data. The EUVI and HMI data are downloaded via the Virtual Solar Observatory and the Joint Science Operations Center. Y. Su acknowledges Dr. Mark Weber for helpful discussions and thanks Dr. Suli Ma for helping on the radial filter technique. This project is partially supported under contract NNM07AB07C from NASA to the Smithsonian Astrophysical Observatory (SAO) and SP02H1701R from LMSAL to SAO as well as NASA grant NNX12AI30G.



## REFERENCES

- Antiochos, S. K., & Klimchuk, J. A. 1991, *ApJ*, 378, 372
- Antiochos, S. K., Dahlburg, R. B., & Klimchuk, J. A. 1994, *ApJ*, 420, L41
- Asgari-Targhi, M., & van Ballegooijen, A. A. 2012, *ApJ*, 746, 81
- Aulanier, G., & Démoulin, P. 2003, *A&A*, 402, 769
- Aulanier, G., DeVore, C. R., & Antiochos, S. K. 2002, *ApJ*, 567, L97
- Aulanier, G., Demoulin, P., van Driel-Gesztelyi, L., Mein, P., & Deforest, C. 1998, *A&A*, 335, 309
- Berger, T. E., Shine, R. A., Slater, G. L., et al. 2008, *ApJ*, 676, L89
- Berger, T. E., Slater, G., Hurlburt, N., et al. 2010, *ApJ*, 716, 1288
- Bobra, M. G., van Ballegooijen, A. A., & DeLuca, E. E. 2008, *ApJ*, 672, 1209
- Bommier, V., Landi Degl’Innocenti, E., Leroy, J.-L., & Sahal-Brechot, S. 1994, *Sol. Phys.*, 154, 231
- Brueckner, G. E., et al. 1995, *Sol. Phys.*, 162, 357
- Canou, A., & Amari, T. 2010, *ApJ*, 715, 1566
- Chae, J. 2010, *ApJ*, 714, 618
- Chae, J., Ahn, K., Lim, E.-K., Choe, G. S., & Sakurai, T. 2008, *ApJ*, 689, L73
- Chae, J., Wang, H., Qiu, J., et al. 2001, *ApJ*, 560, 476
- DeRosa, M. L., et al. 2009, *ApJ*, 696, 1780
- DeVore, C. R., & Antiochos, S. K. 2000, *ApJ*, 539, 954
- Dudík, J., Aulanier, G., Schmieder, B., Bommier, V., & Roudier, T. 2008, *Sol. Phys.*, 248, 29
- Engvold, O. 1976, *Sol. Phys.*, 49, 283
- Foukal, P. 1971, *Sol. Phys.*, 19, 59
- Gaizauskas, V. 1998, *IAU Colloq. 167: New Perspectives on Solar Prominences*, 150, 257

- Gibson, S. E., Foster, D., Burkepile, J., de Toma, G., & Stanger, A. 2006, *ApJ*, 641, 590
- Golub, L., et al. 2007, *Sol. Phys.*, 243, 63
- Guo, Y., Schmieder, B., Démoulin, P., Wiegelmann, T., Aulanier, G., Török, T., & Bommier, V. 2010, *ApJ*, 714, 343
- Heinzl, P., & Anzer, U. 2001, *A&A*, 375, 1082
- Heinzl, P., & Anzer, U. 2006, *ApJ*, 643, L65
- Heinzl, P., Schmieder, B., Fárnik, F., et al. 2008, *ApJ*, 686, 1383
- Hillier, A., Berger, T., Isobe, H., & Shibata, K. 2012, *ApJ*, 746, 120
- Hirayama, T. 1985, *Sol. Phys.*, 100, 415
- Howard, R. A., et al. 2008, *Space Sci. Rev.*, 136, 67
- Jensen, E., & Wiik, J. E. 1990, *IAU Colloq. 117: Dynamics of Quiescent Prominences*, 363, 298
- Kano, R., et al. 2008, *Sol. Phys.*, 249, 263
- Karpen, J. T., Tanner, S. E. M., Antiochos, S. K., & DeVore, C. R. 2005, *ApJ*, 635, 1319
- Kippenhahn, R., & Schlüter, A. 1957, *ZAp*, 43, 36
- Kosugi, T., et al. 2007, *Sol. Phys.*, 243, 3
- Kucera, T. A., Tovar, M., & de Pontieu, B. 2003, *Sol. Phys.*, 212, 81
- Kuperus, M., & Raadu, M. A. 1974, *A&A*, 31, 189
- Labrosse, N., Heinzl, P., Vial, J.-C., et al. 2010, *Space Sci. Rev.*, 151, 243
- Lemen, J. R., Title, A. M., Akin, D. J., et al. 2012, *Sol. Phys.*, 275, 17
- Lin, Y. 2011, *Space Sci. Rev.*, 158, 237
- Lin, Y., Engvold, O. R., & Wiik, J. E. 2003, *Sol. Phys.*, 216, 109
- Lin, Y., Martin, S. F., & Engvold, O. 2008, *Subsurface and Atmospheric Influences on Solar Activity*, 383, 235
- Low, B. C., & Hundhausen, J. R. 1995, *ApJ*, 443, 818

- Low, B. C., & Petrie, G. J. D. 2005, *ApJ*, 626, 551
- Luna, M., Karpen, J. T., & DeVore, C. R. 2012, *ApJ*, 746, 30
- Mackay, D. H., Karpen, J. T., Ballester, J. L., Schmieder, B., & Aulanier, G. 2010, *Space Sci. Rev.*, 151, 333
- Martin, S. F., Bilimoria, R., & Tracadas, P. W. 1994, *Solar Surface Magnetism*, 303
- Martin, S. F. 1998, *Sol. Phys.*, 182, 107
- Martin, S. F., & McAllister, A. H. 1996, *IAU Colloq. 153: Magnetodynamic Phenomena in the Solar Atmosphere - Prototypes of Stellar Magnetic Activity*, 497
- McAllister, A. H., Mackay, D. H., & Martin, S. F. 2002, *Sol. Phys.*, 211, 15
- Menzel, D. H., & Wolbach, J. G. 1960, *S&T*, 20, 252
- Okamoto, T. J., Tsuneta, S., Berger, T. E., et al. 2007, *Science*, 318, 1577
- Parenti, S., Schmieder, B., Heinzl, P., & Golub, L. 2012, *arXiv:1205.5460*
- Pneuman, G. W. 1983, *Sol. Phys.*, 88, 219
- Priest, E. 1989, *Dynamics and Structure of Quiescent Solar Prominences* (Dordrecht: Kluwer)
- Priest, E. R., Hood, A. W., & Anzer, U. 1989, *ApJ*, 344, 1010
- Rust, D. M., & Kumar, A. 1994, *Sol. Phys.*, 155, 69
- Régnier, S., & Priest, E. R. 2007, *A&A*, 468, 701
- Régnier, S., Amari, T., & Kersalé, E. 2002, *A&A*, 392, 1119
- Savcheva, A., & van Ballegoijen, A. 2009, *ApJ*, 703, 1766
- Savcheva, A.S., & van Ballegoijen, A.A., & DeLuca, E.E. 2012, *ApJ*, 744, 78
- Savcheva, A., Pariat, E., van Ballegoijen, A., Aulanier, G., & DeLuca, E. 2012, *ApJ*, 750, 15
- Schmieder, B., Lin, Y., Heinzl, P., & Schwartz, P. 2004, *Sol. Phys.*, 221, 297
- Schou, J., Scherrer, P. H., Bush, R. I., et al. 2012, *Sol. Phys.*, 275, 229

- Su, Y., Surges, V., van Ballegooijen, A., DeLuca, E., & Golub, L. 2011, *ApJ*, 734, 53
- Su, Y., van Ballegooijen, A., & Golub, L. 2010, *ApJ*, 721, 901
- Su, Y., van Ballegooijen, A., Schmieder, B., Berlicki, A., Guo, Y., Golub, L., & Huang, G. 2009, *ApJ*, 704, 341
- Su, Y., van Ballegooijen, A., Lites, B. W., Deluca, E. E., Golub, L., Grigis, P. C., Huang, G., & Ji, H. 2009, *ApJ*, 691, 105
- Su, Y., van Ballegooijen, A. 2012, *ApJ*, submitted
- Thompson, W.T., *Sol. Phys.*, submitted
- Tandberg-Hanssen, E. 1995, *The nature of solar prominences* Dordrecht: Kluwer
- van Ballegooijen, A. A. 2004, *ApJ*, 612, 519
- van Ballegooijen, A. A., & Cranmer, S. R. 2010, *ApJ*, 711, 164
- van Ballegooijen, A. A., & Martens, P. C. H. 1989, *ApJ*, 343, 971
- van Ballegooijen, A. A., Priest, E. R., & Mackay, D. H. 2000, *ApJ*, 539, 983
- Wuelser, J.-P., et al. 2004, *Proc. SPIE*, 5171, 111
- Yang, W. H., Sturrock, P. A., & Antiochos, S. K. 1986, *ApJ*, 309, 383
- Zirker, J. B., Engvold, O., & Martin, S. F. 1998, *Nature*, 396, 440

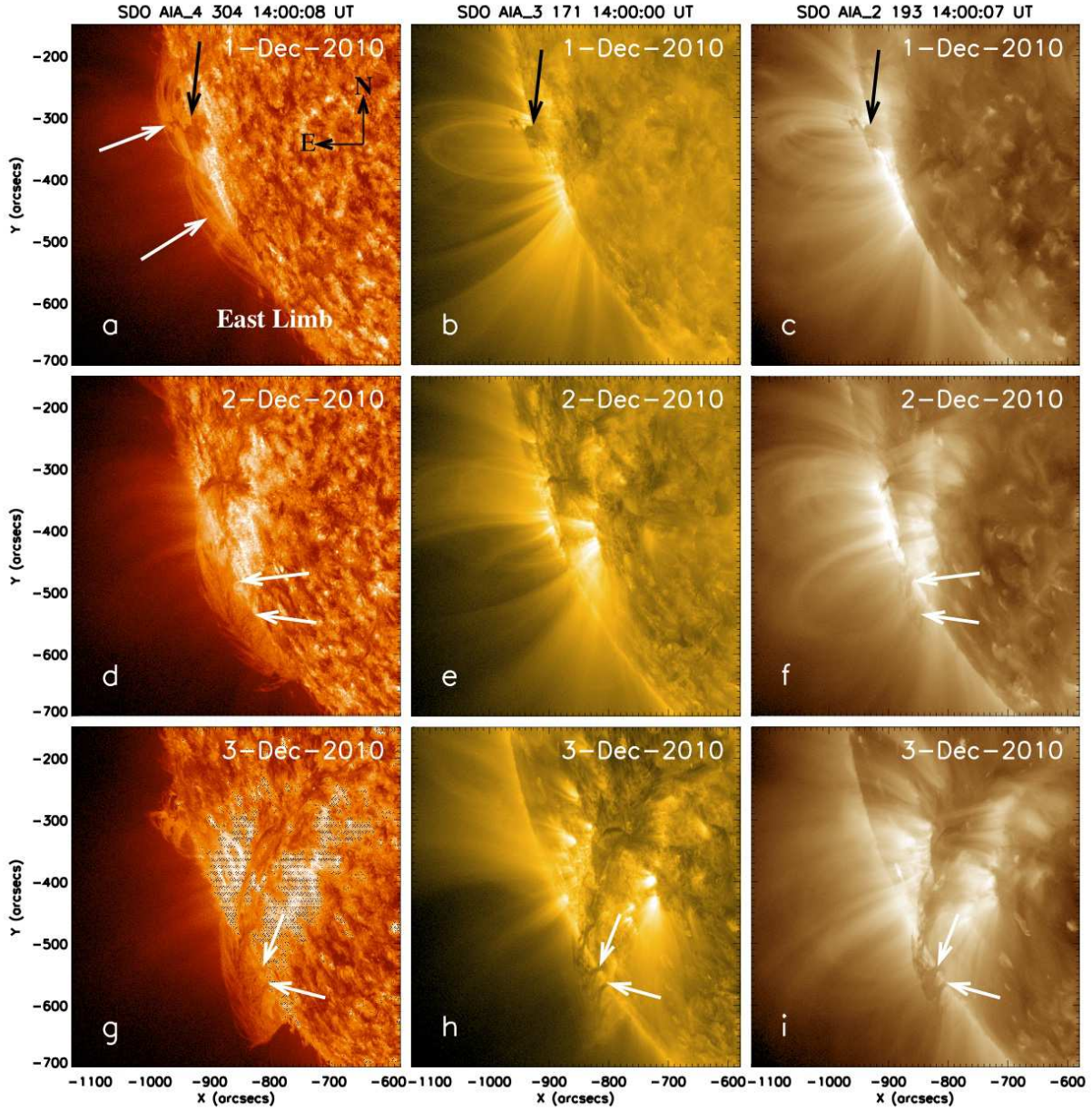


Fig. 1.— SDO/AIA observations of the quiescent prominence at 14:00 UT on 2010 December 1 (top row), December 2 (middle row), and December 3 (bottom row). (A color version of this figure is available in the online journal.)

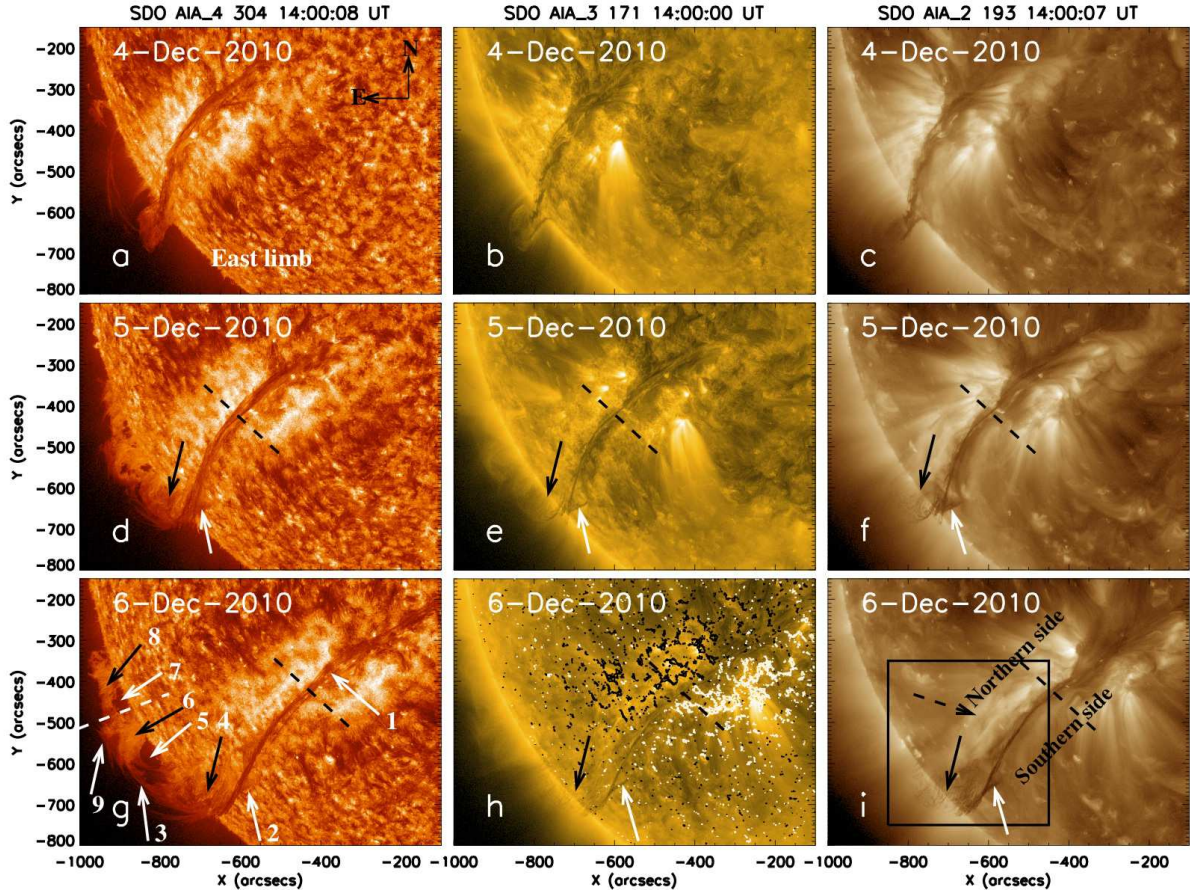


Fig. 2.— SDO/AIA observations of the quiescent prominence at 14:00 UT on 2010 December 3 (top row), December 4 (middle row), and December 5 (bottom row). The white and black contours refer to the positive and negative polarities as observed by SDO/HMI at 14:00 UT on 2010 December 6. (A color version of this figure is available in the online journal.) AIA observations of the prominence at 193 Å and 304 Å within 24 hours before the eruption are also available (video 1) in the electronic edition of the *Astrophysical Journal*. The field of view of the online video contains only the prominence near the limb. The images are also rotated for 120 degree in the clockwise direction.

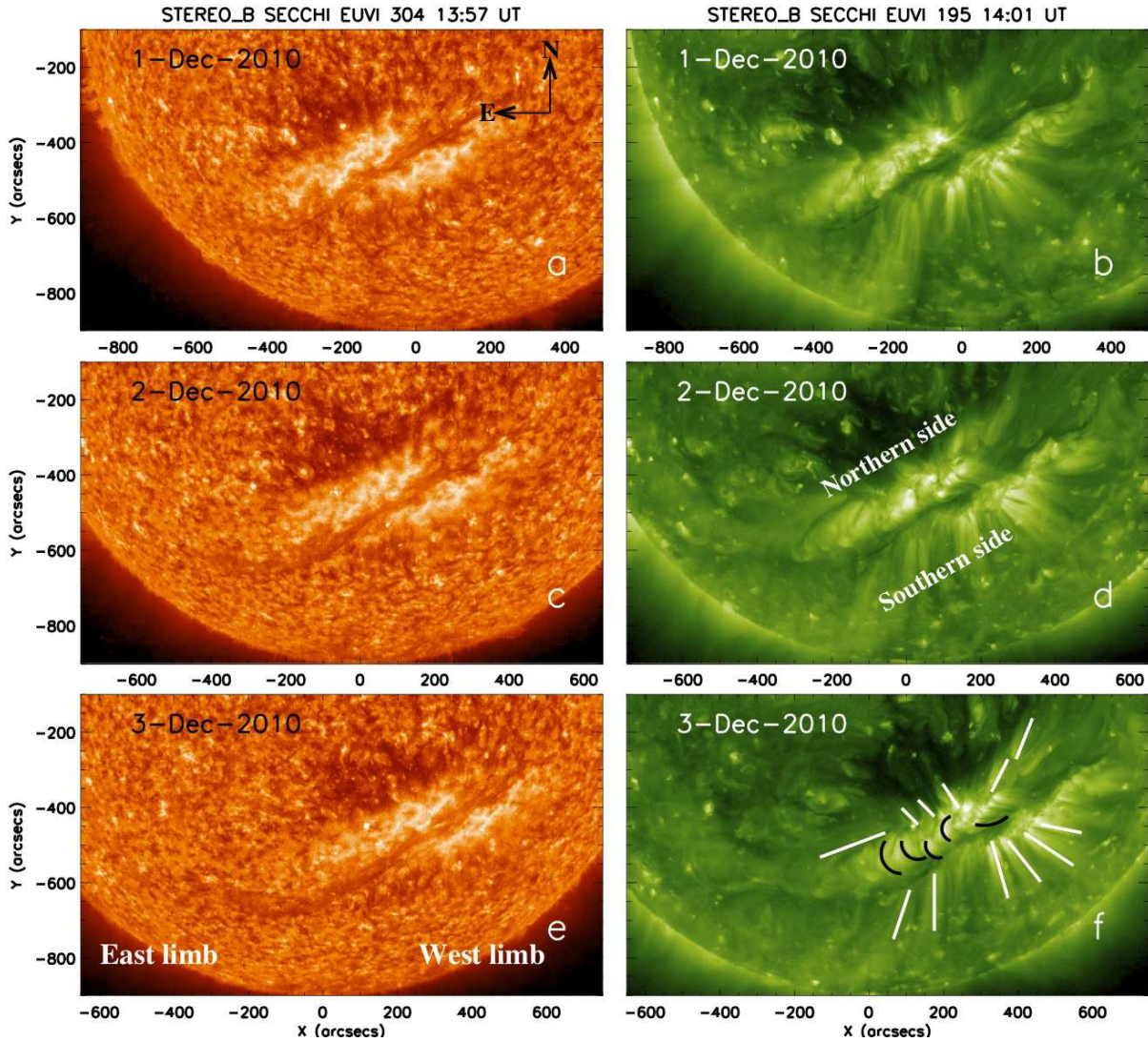


Fig. 3.— STEREO\_BB EUVI observations of the quiescent prominence around 14:00 UT on 2010 December 1 (top row), December 2 (middle row), and December 3 (bottom row). (A color version of this figure is available in the online journal.)

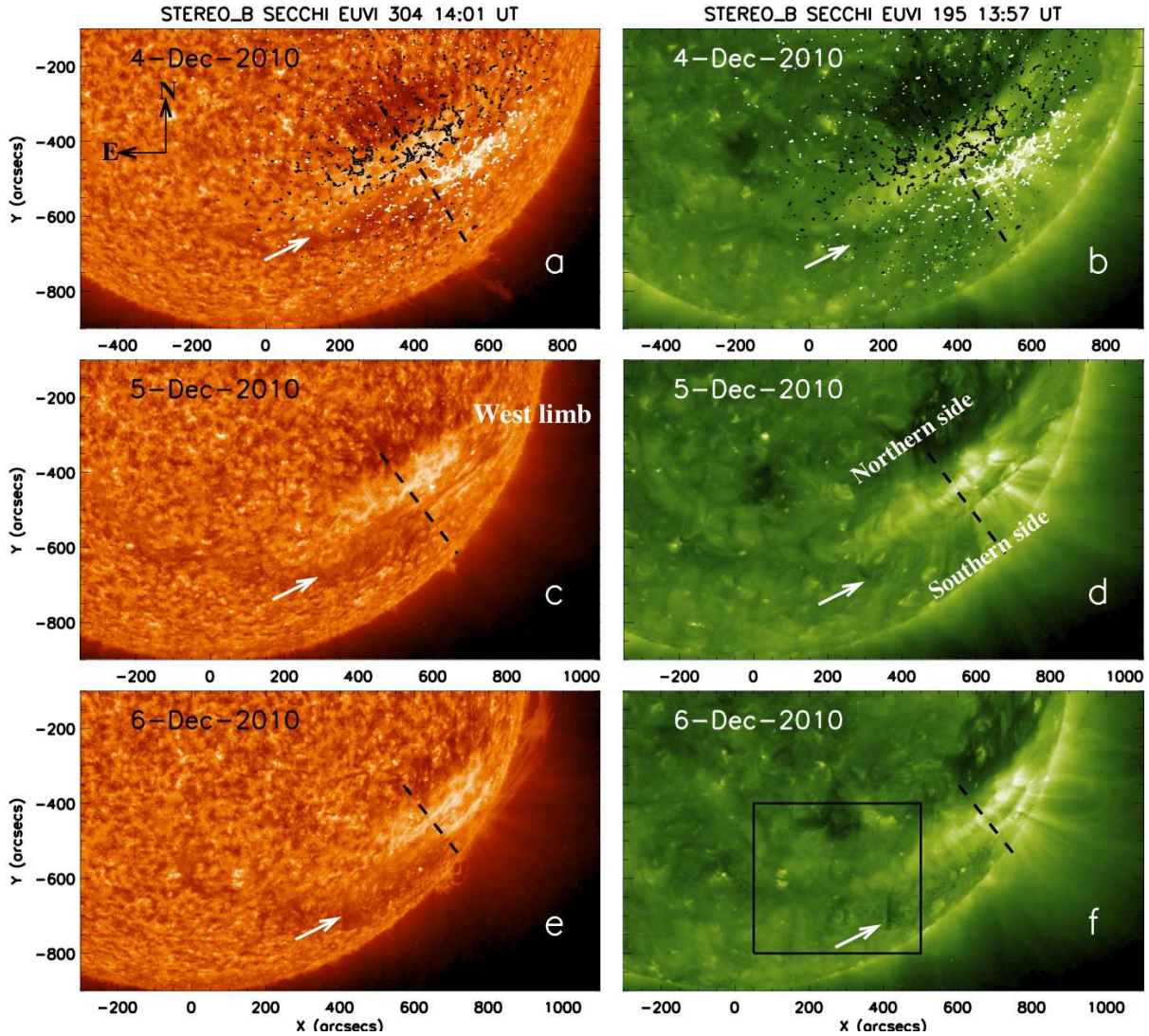


Fig. 4.— STEREO\_B/EUVI observations of the quiescent prominence around 14:00 UT on 2010 December 4 (top row), December 5 (middle row), and December 6 (bottom row). The white and black contours refer to the positive and negative polarities as observed by SDO/HMI at 14:00 UT on 2010 December 6. (A color version of this figure is available in the online journal.) STEREO\_B observations of the prominence at 193 Å and 304 Å within 24 hours before the eruption are also available (video 2) in the electronic edition of the *Astrophysical Journal*.



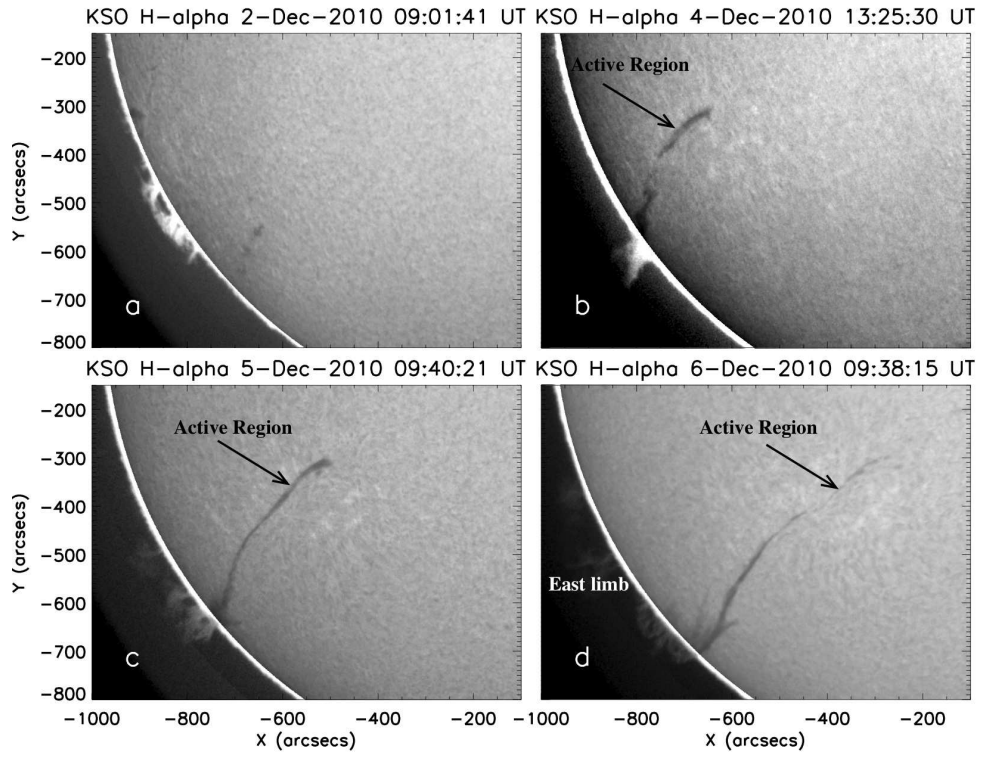


Fig. 5.— KSO H $\alpha$  observations of the quiescent prominence from December 2 to December 6.

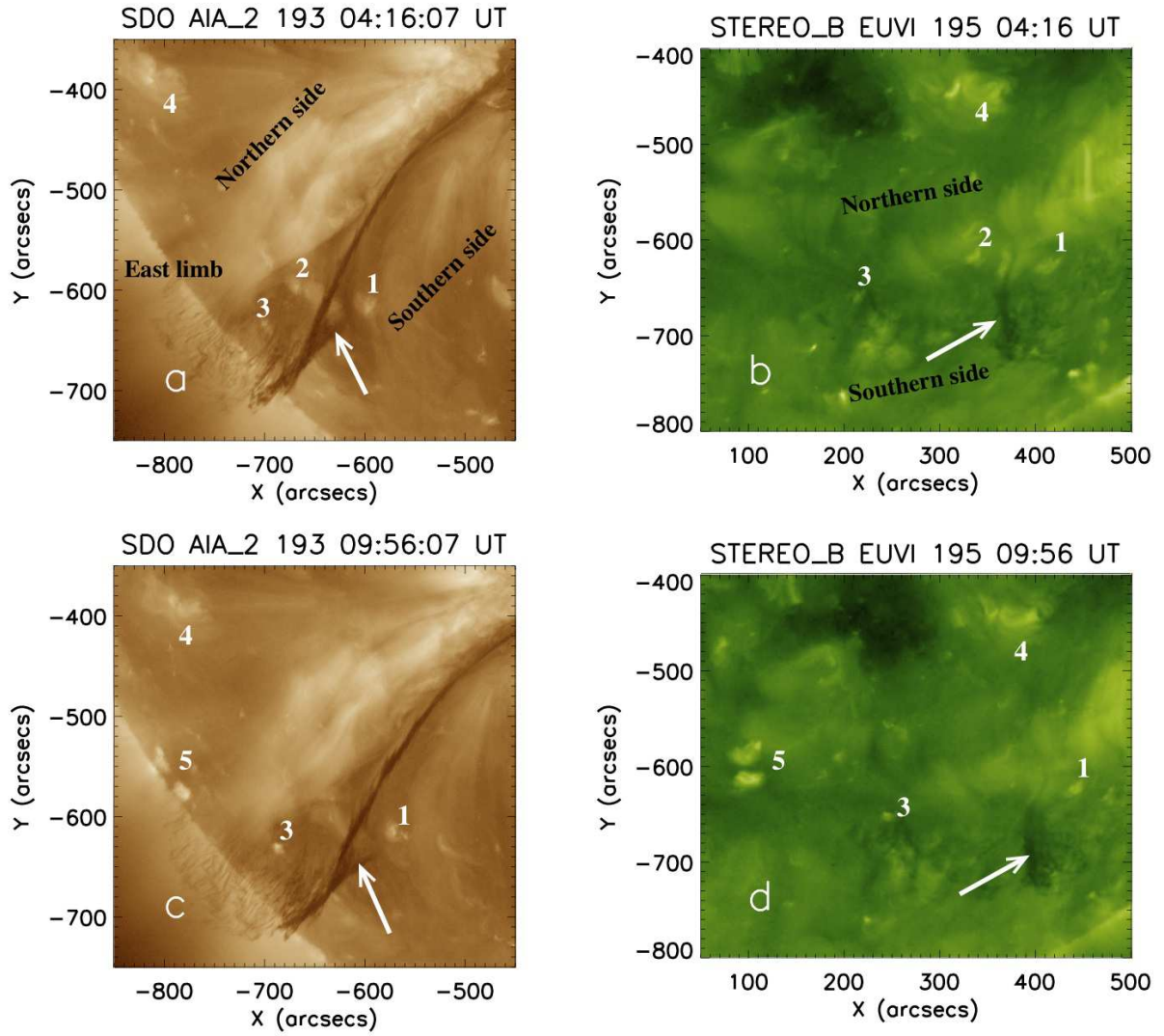


Fig. 6.— SDO/AIA (left column, 193 Å) and STEREO\_B/EUVI (right column, 195 Å) observations of the dense column structure on 2010 December 6 prior to the eruption. (A color version of this figure is available in the online journal.)

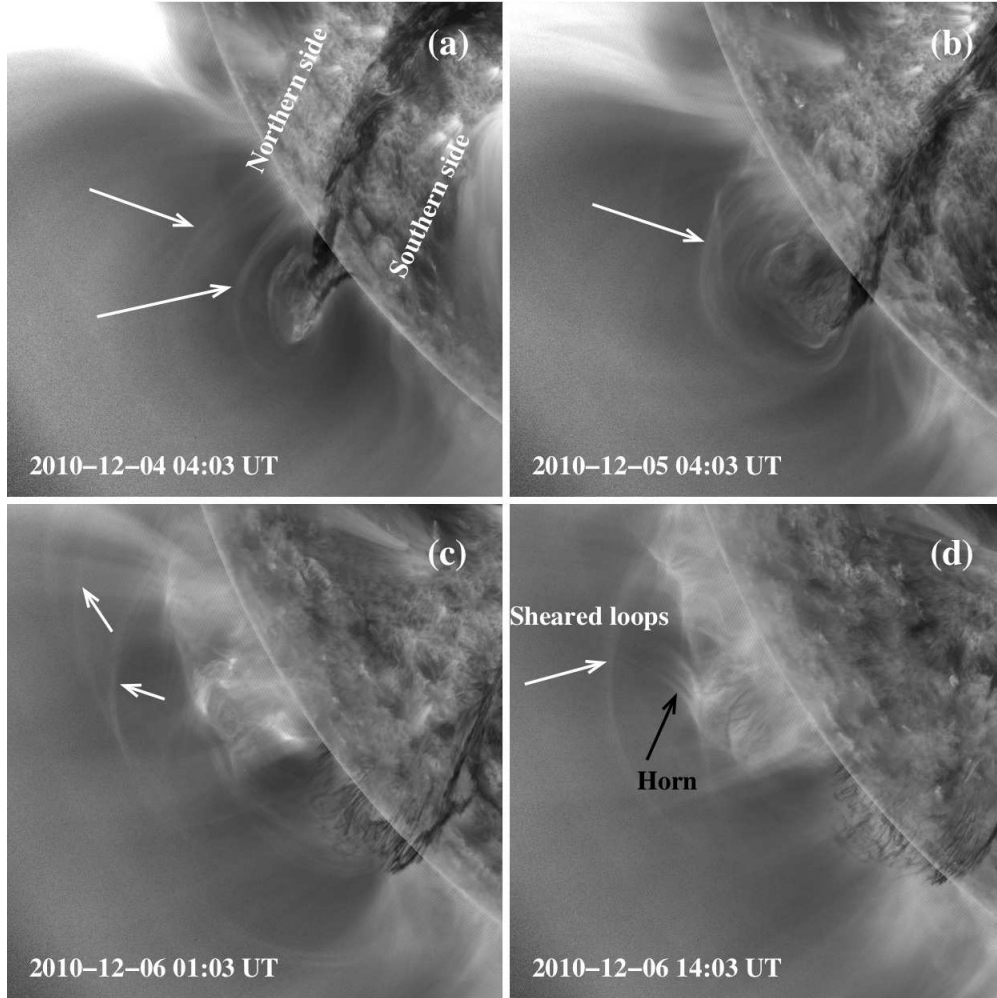


Fig. 7.— SDO/AIA 171 Å observations of loops surrounding the prominence prior to the eruption. Each image is the average of 30 images taken within 6 minutes. All images are contrast enhanced using a radial filter technique developed by S. Cranmer (2010, private communication). The field of view of each image is  $540'' \times 540''$ . An animation of this figure (video 3) is available in the online journal. Note that radial filter technique is not applied for the animation.

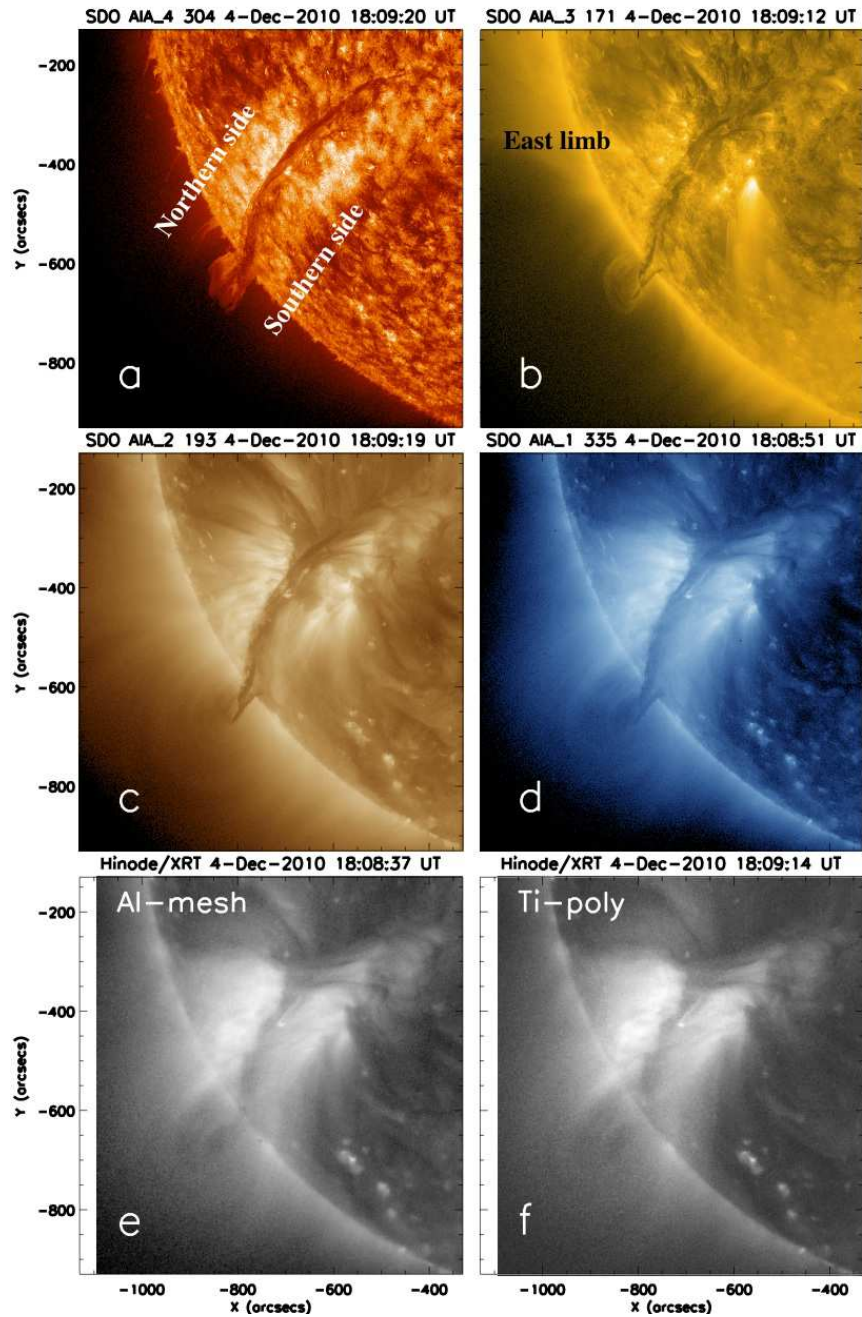


Fig. 8.— Multi-channel observations of the cavity structure around 18:09 UT on 2010 December 4. The images in the top two rows are provided by SDO/AIA, while Hinode/XRT images are shown in the bottom row. (A color version of this figure is available in the online journal.)

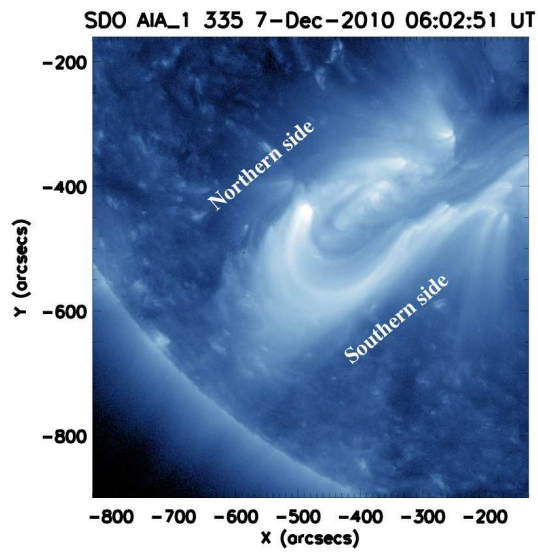


Fig. 9.— SDO/AIA (left column) of the post-eruption loops at 335 Å on 2010 December 7. (A color version of this figure is available in the online journal.)

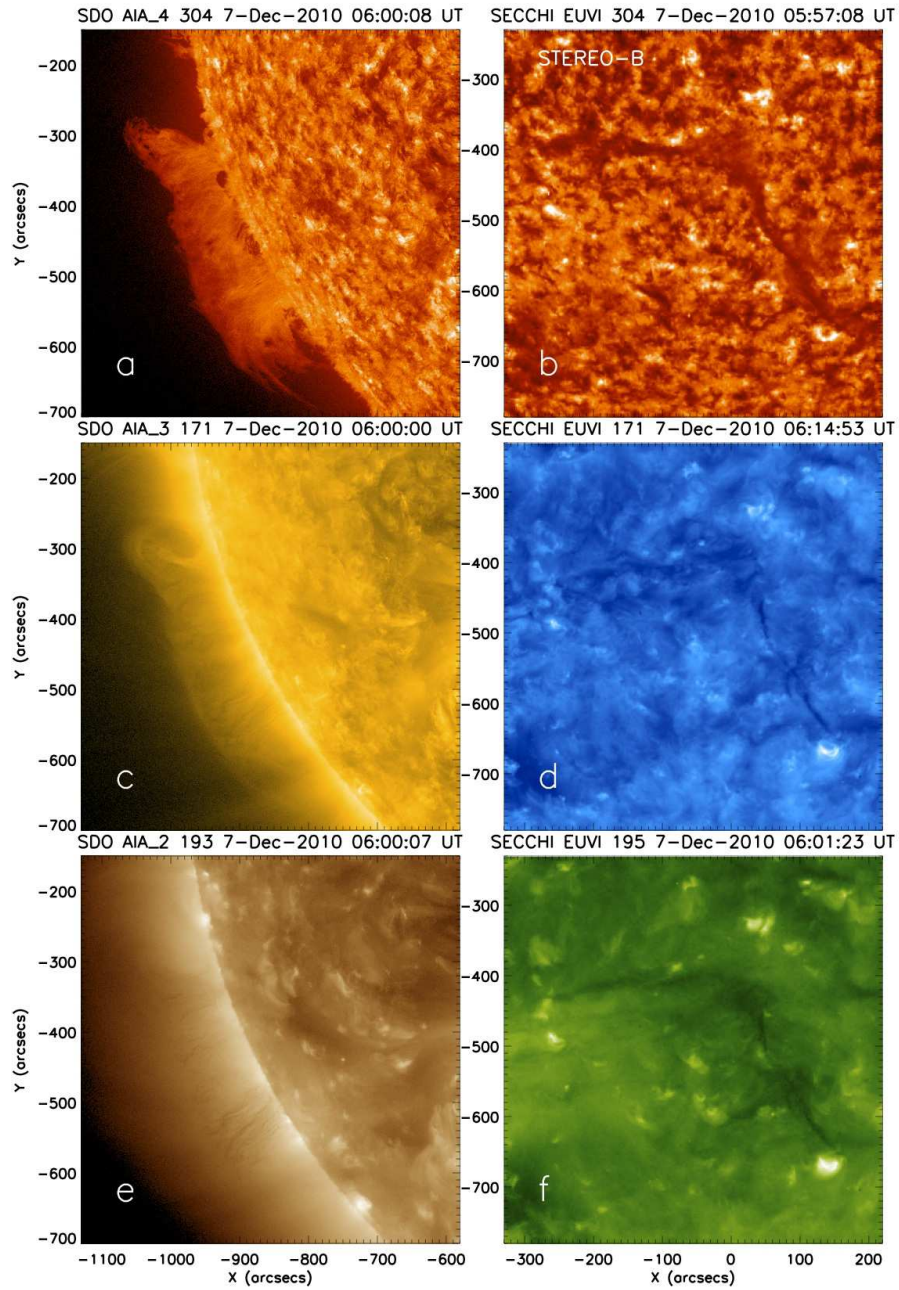


Fig. 10.— SDO/AIA (left column) and STEREO\_B/EUVI (right column) observations of the prominence after the eruption. The images at the top, middle, and bottom rows are taken at 304 Å, 171 Å, and 193/195 Å on 2010 December 7, respectively. (A color version of this figure is available in the online journal.)

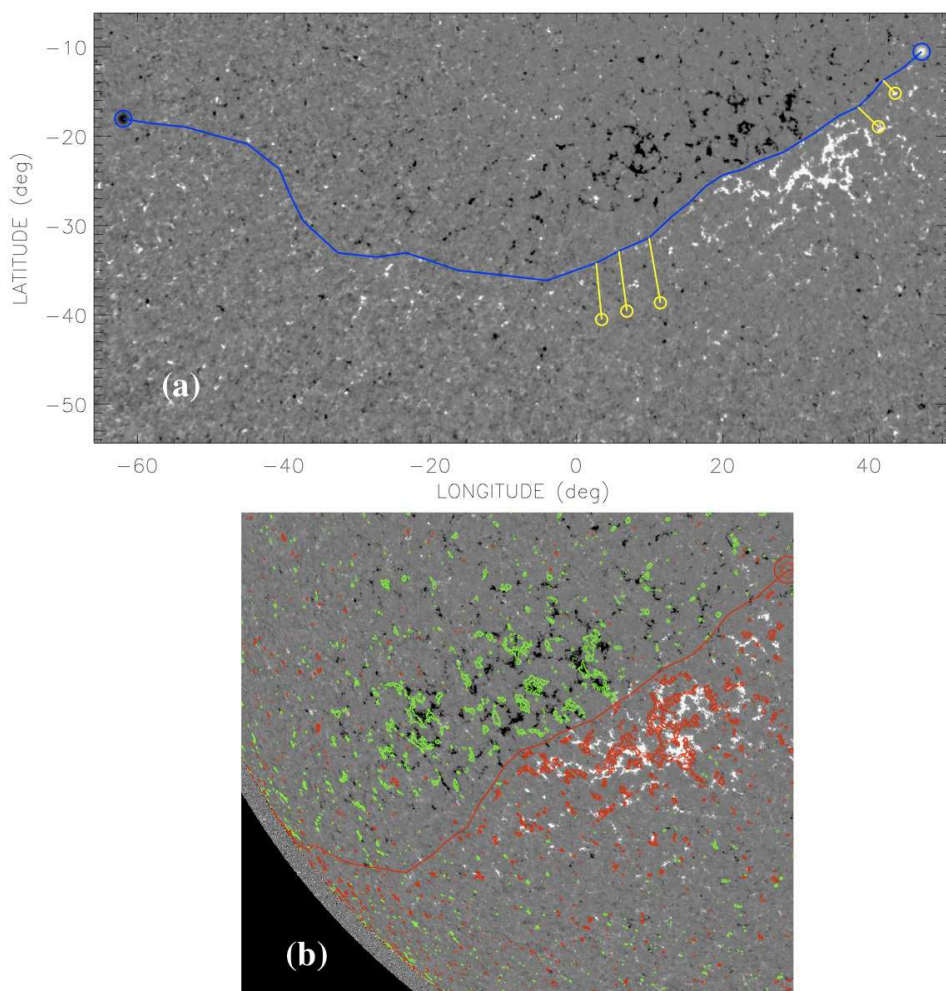


Fig. 11.— (a) Longitude-latitude map of the radial component of magnetic field in photosphere in the HIRES region of the model. The zero-point of the longitude corresponds to the central meridian on 2010 December 10 at 14:00 UT. The blue curve shows the path along which the flux rope is inserted into the model. Extra axial fluxes are added to (right) or removing from (left) the flux rope along places indicated by the yellow bars. (b) The magnetic map shown in (a) (red and green contours) is overlaid on the HMI magnetogram taken at 14:00 UT on 2012 December 6 (black and white image). The path along which the flux rope is inserted is shown as red curve in this image. Note that there is no systematic change in the flux distribution from December 6 to December 10.

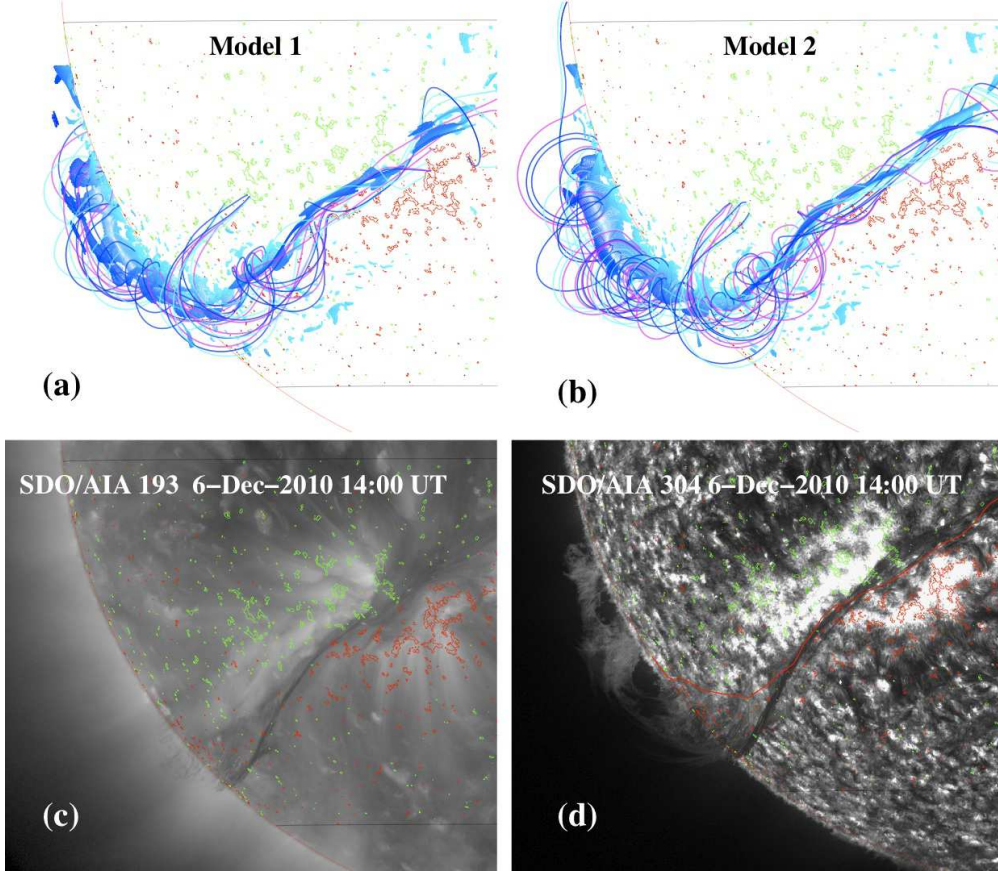


Fig. 12.— Three-dimensional magnetic models of a quiescent prominence observed with SDO/AIA on 2010 December 6 at 14:00 UT. The top panels show results from two NLFFF models constructed using the flux rope insertion method. For the model in panel (a) the axial flux of the flux rope  $\Phi_{\text{axi}} = 2 \times 10^{20}$  Mx, and the initial poloidal flux  $F_{\text{pol}} = 1 \times 10^{10}$  Mx cm $^{-1}$ , which produces a relatively small degree of twist. Panel (b) shows a model with the same axial flux but larger twist ( $F_{\text{pol}} = 2 \times 10^{10}$  Mx cm $^{-1}$ ). The colored curves are magnetic field lines in and near the flux rope, the blue features indicate field-line dips, and the red/green contours show the photospheric flux distribution ( $B_r = \pm 71$  G, respectively). The red arc is the east solar limb, and the black lines are the latitudinal boundaries of the HIRES domain. These features are projected onto the plane of the sky as seen from the SDO spacecraft at 14:00 UT. Panels (c) and (d) show AIA images taken in the 193 Å and 304 Å passbands. The path along which the flux rope is inserted is shown as red curve in (d). Note that just inside the limb the real prominence is displaced to the south with respect to the PIL. This displacement is not reproduced in the NLFFF models.



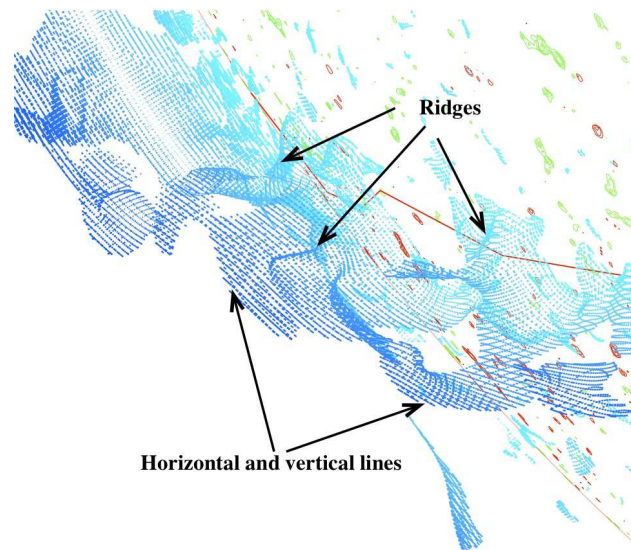


Fig. 13.— Zoomed in view of the field line dips from Model 1 as shown in Figure 12a near the east limb (red arc). The red and green contours refer to the photospheric flux distribution. The red curve refers to the path along which the flux rope is inserted.

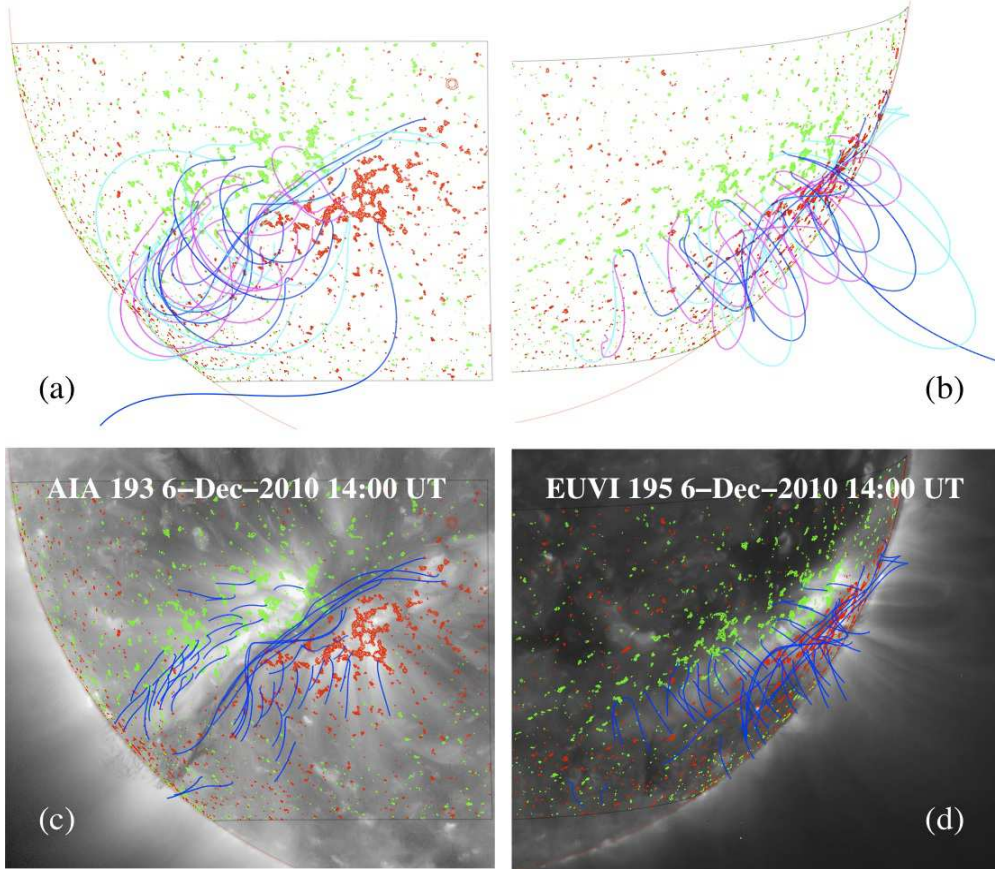


Fig. 14.— Comparison of the model with SDO/AIA and STEREO\_BB/EUVI observations of the coronal arcade surrounding the prominence cavity (model with poloidal flux  $F_{\text{pol}} = 10^{10} \text{ Mx cm}^{-1}$ ). The top panels show the same set of field lines (colored curves) seen from two different viewpoints: (a) SDO and (b) STEREO\_B on 2010 December 6 at 14:00 UT. The red and green contours show the photospheric flux distribution ( $B_r = \pm 71 \text{ G}$ , respectively), and the red arcs indicate the east and west limbs. The bottom panels show images in (c) AIA 193 Å and (d) EUVI 195 Å, which are dominated by Fe XII 195 Å emission. The images show thin threads and fans that presumably are aligned with the local magnetic field. On the quiet Sun the emissivity in the Fe XII line drops off rapidly with height (due to gravitational stratification of the plasma), so only the plasma on the lower parts of the field lines is observable. Therefore, we overplot the lower parts of the field lines that lie at heights  $h < 0.07 R_{\odot}$  (blue line segments). Note that the orientation of these line segments is consistent with the observed fine structures, indicating the model reproduces the fields in the coronal arcade.

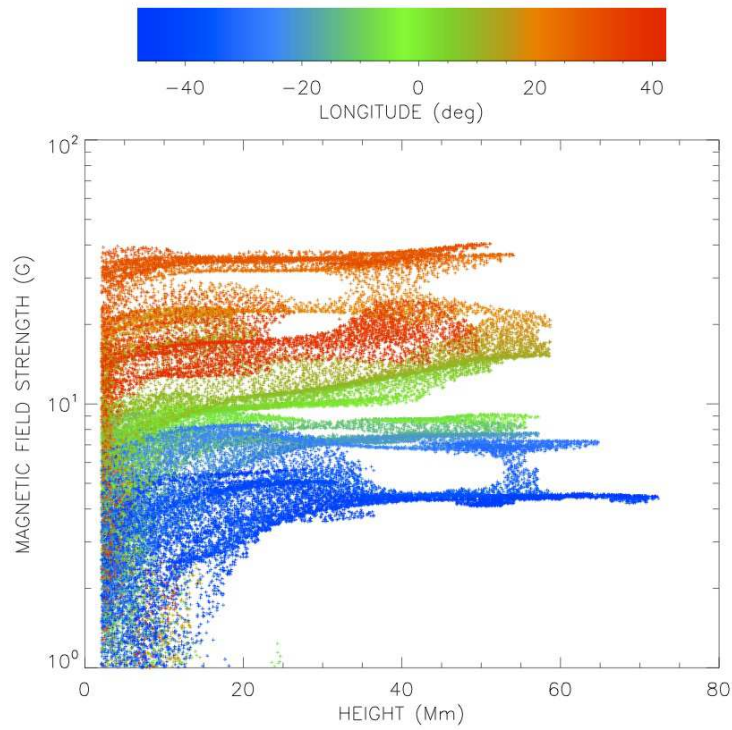


Fig. 15.— Magnetic field strength at dips in the field lines from Model 1 are plotted as function of the height of the dips above the photosphere. The prominence plasma is assumed to be located as such dips. All positions along the filament channel are included in this plot, except the two ends of the flux rope where the rope is anchored in the photosphere. Different colors represent the field strength at different longitudes as shown in Figure 11a.

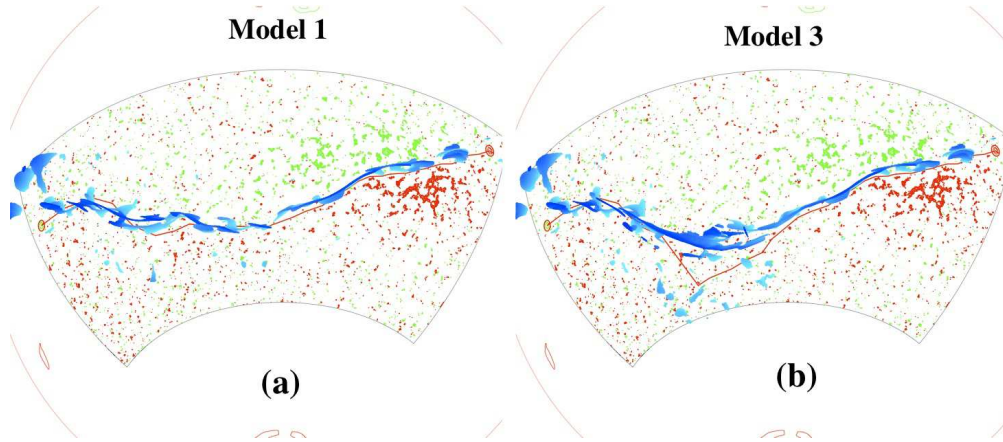


Fig. 16.— Top view of the field line dips (blue features) from Model 1 and Model 3. Model 3 has the same parameters as Model 1 except the filament path (red curve). The red and green contours refer to the photospheric flux distribution.

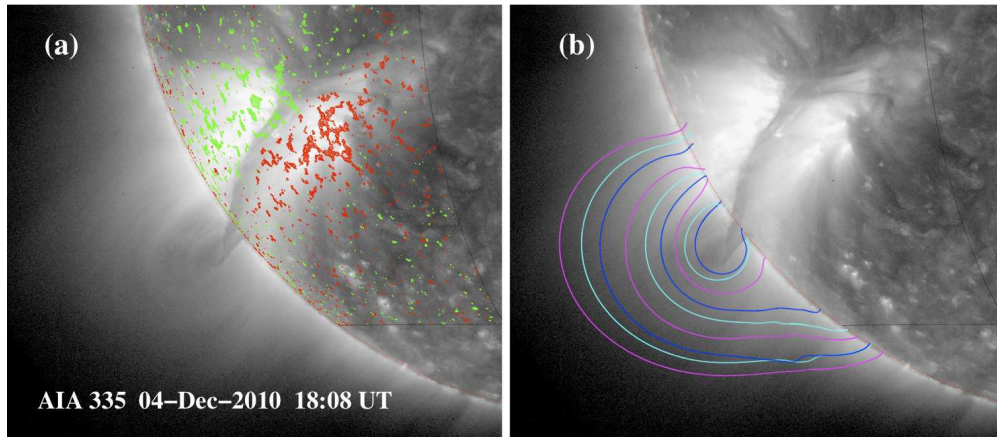


Fig. 17.— Comparison of the observed cavity and magnetic field lines from Model 1. (a) SDO/AIA image of the cavity at 18:08 UT on 2010 December 4. The red and green contours refer to photospheric magnetic fields observed by SDO/HMI. (b) The same image as in (a) overlaid with magnetic field lines (color lines) surrounding the flux rope from Model 1.